Constraints on Saturn's E Ring from the Voyager 1 Radio Astronomy Instrument

NICOLE MEYER-VERNET

Département de Recherche Spatiale, CNRS URA 264, Observatoire de Paris, 92195 Meudon Cedex, France
E-mail: meyer@obspm.fr

ALAIN LECACHEUX

Département ARPEGES, CNRS URA 1757, Observatoire de Paris, 92195 Meudon Cedex, France

AND

BENT M. PEDERSEN

Département ARPEGES, CNRS URA 1757, Observatoire de Paris, 92195 Meudon Cedex, France; and CNRS/INSU,
3 rue Michel Ange, 75766 Paris Cedex 16, France

We have reanalyzed the data acquired by the planetary radio-astronomy (PRA) experiment during the passage of Voyager 1 through Saturn's E ring. Depending on the distance from the ring plane, the instrument detected (i) dust grain impacts on the spacecraft and/or (ii) plasma waves or noise. The signal produced by the dust can be recognized by its power spectrum. It is dominant in a region of $\approx$12,000 km vertical extent around the ring plane, and has a maximum at roughly 5000 km southward of equator (at 6.1 R_S from Saturn). Assuming that the grain concentration is given by the model of Showalter *et al.* (Showalter, M. R., J. N. Cuzzi, and S. M. Larson 1991. *Icarus* **94**, 451–473) derived from optical observations, we infer from the mean PRA voltage and from the histogram of the data that the particles have a mean radius $r \approx 1 \mu$m and a narrow size distribution of fractional dispersion between 10 and 30%. These values agree with the above model. We have also investigated the ring thickness. The PRA signal has a full vertical width at half-maximum of $\approx$8000 km, which is 2.3 times less than that given by the optical model. Since the signal produced by the dust varies strongly with the grain size (as r^6), our measurements can be made compatible with the optical observations if the particle mean size decreases slightly with vertical distance, by about 10% over 4000 km.   © 1996 Academic Press, Inc.

1. INTRODUCTION

Saturn's E ring is believed to be made of dust, like the other etheral rings encircling the four gas giant planets. The satellite Enceladus might be the main source of dust for this ring (Hamilton and Burns 1994). In contrast to the dense main rings where collisions and collective processes play an important role, the particle concentration is so small in these faint rings that the grains behave independently of each other, being mainly subjected to electromagnetic forces, light pressure, and other nongravitational perturbations, in addition to the usual gravitational forces (Burns *et al.* 1984). This makes these etheral rings good places to study the fundamental processes governing trajectories of individual particles under these conditions. On the practical side, studying the E ring is crucial to determine a safe trajectory for the Cassini orbiter, which will spend a long time there.

Its faintness makes this ring difficult to observe, and a large bulk of data is necessary in order to build a consistent picture. Three main kinds of measurements are available: (i) optical observations, which have the interest of being also feasible from Earth, but can only reveal properties integrated along the line of sight, (ii) *in situ* observations of dust impacts, which have the interest of being local, but have a limited space coverage since they can only be made along the trajectory of available space probes, and (iii) absorption signatures on spacecraft-based charged particle experiments, which are rather indirect, without having any of the above advantages.

Showalter *et al.* (1991) have produced a three-dimensional model based on a large subset of the available optical data for the E ring, obtained both from the ground and during the Voyager encounters. Although not unique owing to the line-of-sight integration and to the limited number of viewing geometries and wavelengths, this model is

113

the most complete so far. Its major findings are: a narrow distribution of particles of radius 1.0 ± 0.3 μm, a density peak at Enceladus orbit, and a general increase in vertical thickness with distance from Saturn.

Apart from two impacts recorded by the Pioneer 11 meteoroid detector (Humes *et al.* 1980), the *in situ* observations of the E ring have been made by the radioastronomy (PRA) and plasma wave (PWS) instruments aboard Voyager 1, which crossed the ring plane near Dione orbit. This spacecraft did not carry conventional dust detectors, but the above instruments replaced them in some way by recording the signals due to dust impacts on the spacecraft body and its antennae. Basically, when a dust grain impacts a solid target with a velocity larger than a few km/sec, the available kinetic energy is sufficient to vaporize and ionize the grain. This produces an expanding plasma cloud, and a fraction of the released charge is recollected, and then detected by the antennae. Both instruments detected dust in this way near the ring planes of Saturn (Aubier *et al.* 1983, Gurnett *et al.* 1983, Tsintikidis *et al.* 1994, 1995), Uranus (Meyer-Vernet *et al.* 1986a, Gurnett *et al.* 1987), and Neptune (Gurnett *et al.* 1991, Pedersen *et al.* 1991).

The main problem with these instruments is that it was not anticipated that they would record dust, so that they were not designed nor calibrated for this purpose. Hence, in order to infer the grain mass from the charge released, one has to rely on calibration of conventional dust detectors, which work under rather different conditions. This problem holds for both PRA and PWS, but the case of PWS is still worse since its response to the released charge itself is unknown, so that it is dependent on PRA for calibration (we shall return to this point in Section 5).

Within the E ring, these *in situ* observations were difficult to interpret, since the signal recorded was not only produced by the dust but also by the ambient plasma. In this paper we reexamine the PRA data, first published by Aubier *et al.* (1983), and we are able to separate the dust and plasma effects by their different spectra. This allows us to study in detail the data in the interval where they are mainly produced by the dust. In Section 2, we review the calibration of the PRA instrument and the observations. In Section 3, we show how the dust properties can be inferred from the data. In Section 4, we infer the corresponding dust grain parameters and compare them with those given by the optical model. In Section 5, we comment on the PWS results. Finally, the implications of the present work are summarized and discussed in Section 6.

Unless otherwise stated, we use the international system of units. All times are spacecraft event UT time.

2. PRA OBSERVATIONS

2.1. The PRA Instrument and Calibrations

The PRA instrument (Warwick *et al.* 1977) consists of a pair of orthogonal monopoles, loaded against the conduc-
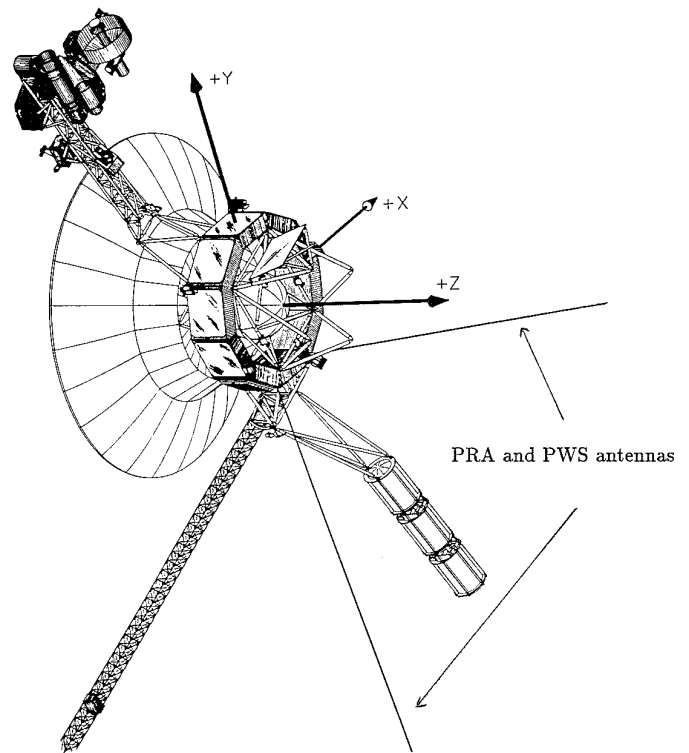

FIG. 1. The Voyager spacecraft. The wire antennae are used in monopole configuration by PRA, and in dipole configuration by PWS; they are made of Be–Cu tubes having 10 m length and 0.63 cm radius; they are mutually orthogonal and perpendicular to the 13-m length magnetometer boom, which is tilted by 50° from the $-Z$ axis and contained in the Y–Z plane. The diameter of the telemetry antenna is 3.6 m.

tive structure of the spacecraft and connected to a very sensitive broad-band receiver. The monopoles are cylinders of length $L = 10$ m and radius $a = 0.63$ cm, implanted on the spacecraft as shown in Fig. 1.

The receiver is swept through the full frequency range (1.2 kHz–40.5 MHz) every 6 sec, dwelling at each of the 198 frequency channels for $\delta t = 25$ msec. We use in this study the channels below 100 kHz of the low-frequency band, whose spacing is 19.2 kHz and bandwidth is 1 kHz.

The calibration of the instrument is described in the Appendix. We use two independent methods: (i) preflight calibrations, and (ii) common observations of solar bursts by PRA and the radio receiver on the spacecraft ISEE-3 (Lecacheux *et al.* 1989), completed by recent rheographic measurements of the electric length of the antennae with a scale model of the Voyager spacecraft (Lecacheux and Manning 1995).

Both methods give the same instrument calibration

$$V_0^2 = V^2 \times 4/\Gamma^2 = 10^{-17} \times 10^{x/10}. \tag{1}$$

Here, x is the telemetered and calibrated signal (in dB)

measured at the input of the PRA receiver, V^2 the voltage power spectral density on one monopole in the low-frequency band, and Γ^2 the receiver's transfer gain. We have written the calibration in this form because $\Gamma^2 \approx 4$ for the measurements for which the receiver was designed. This is so because the base capacitance of the antenna mounting structure, C_b, is roughly equal to the antenna capacitance, so that the voltage at the receiver ports is halved (Lang and Peltzer 1977). In the present study, however, the receiver is used to measure voltages on the spacecraft, whose capacitance is $C \gg C_b$, so that $\Gamma^2 \approx 1$, whence

$$V_0^2 = 4V^2. \tag{2}$$

Note that this calibration holds for signals much above the receiver noise, which is the case in the present study.

2.2. Observations

Figure 2 shows the observed voltage spectral density V_0^2 in the 20.4 kHz channel as a function of time, during the passage of Voyager 1 through the E ring on November 13, 1980. The other channels below 100 kHz display similar behavior (except the lowest channel at 1.2 kHz, which is partially saturated).

The lower panel shows the corresponding spacecraft trajectory projected in a meridian plane of Saturn. Near the equatorial plane crossing, the spacecraft velocity in cylindrical coordinates centered at Saturn is

$$v_\rho = 16.7 \text{ km/sec}, \quad v_z = 8.1 \text{ km/sec}, \quad v_\phi = 9.5 \text{ km/sec}.$$

The voltage has a narrow peak at ≈ 4.2 hr (6.1 R_S from Saturn), which is centered ≈ 0.08 R_S below the equatorial plane. This narrow peak is surrounded by a much broader structure. We have not plotted the data at earlier and later times because they are polluted by the Saturn kilometric radio emissions, which are recognized by their characteristic polarization properties (Kaiser et al. 1984). Note that all data show considerable intensity scatter—a fact that we will exploit in Section 4.2.

In order to identify the origin of the signal, we first study its spectrum. Figure 3 shows the voltage power spectrum near 3.6 hr (within the 12 min period 3.5–3.7 hr). It varies as $V_0^2 \propto f^{-2}$ below 100 kHz. At higher frequencies, the signal is polarized and we attribute it to Saturn kilometric radio emissions. All the spectra in the broad structure surrounding the peak shown in Fig. 2 have roughly the same spectral index. Such an f^{-2} voltage power spectrum is characteristic of shot noise; this is easily understood since the Fourier transform of a step function varies as f^{-1}, whose square is f^{-2}. In practice, this spectral shape is produced by uncorrelated pulses $V(t)$ whose rise time is much smaller than the inverse $1/f$ of the observing frequency (and the

decay time much larger than $1/f$). Impacts of the ambient electrons or ions on the spacecraft body or the antennae (or photoelectron emission) generally produce such a spectrum below the plasma frequency (see Meyer-Vernet 1983, 1985). This spectral index may also be obtained with plasma instabilities or noise with rise and decay times having such a property. We thus attribute the signal in the wide structure surrounding the narrow peak to the ambient plasma.

Close to the planetary equator, the signal has a very different spectrum. In Fig. 4 we have plotted the power spectral density observed at the center of the peak (within the 12 min period 4.1–4.3 hr). In order to estimate how the plasma noise might perturbate the measured voltage, we have superimposed to the data the mean observed spectrum due to the plasma (already plotted in Fig. 3). The plasma noise can be neglected at 20.4 kHz, but becomes increasingly important at higher frequencies. To tentatively correct our data for this effect, we have substracted this plasma noise from the measured average spectrum. The result is plotted as big black dots. The spectral shape is close to $V_0^2 \propto f^{-3}$ for $f \lesssim 100$ kHz. Farther from the equator, the signal is highly polarized at higher frequencies, and we attribute it to Saturn radio emissions. A similar spectral index is found for all the spectra within the peak surrounding the ring plane ($4.0 < t < 4.4$ hr). This observed spectrum is less steep than the f^{-4} voltage power spectrum produced above several kHz by dust impact ionization (Aubier et al. 1983, Meyer-Vernet 1985). This discrepancy suggests that the plasma noise is somewhat larger near the ring plane than farther out, so that the observed spectrum is polluted at the highest frequencies. We thus attribute the observations in the time interval $4.0 < t < 4.4$ hr to impacts of dust grains on the spacecraft body and on the antennae (plus a contribution of plasma noise at high frequencies).

This interpretation of the narrow and wide structures as mainly produced by dust and plasma, respectively, is supported by our knowledge of the Saturn environment. The width of the narrow peak in the direction perpendicular to the ring plane is on the order of magnitude of a tenth of Saturn's radius R_S; this is the order of magnitude of the E ring's width near 6 R_S from Saturn (Showalter et al. 1991). On the other hand, the width of the broad structure is on the order of R_S; this is the order of magnitude of the plasma disk's width at this distance from Saturn (Richardson and Sittler 1990). We will study these points more precisely in Sections 3 and 4, and we will infer grain parameters from the data mainly produced by dust impacts, using two different methods to verify the consistency of the results. We will use the spectral amplitude to infer the mean particle size, and the scatter of the data to infer the width of the particle size distribution. Finally, the profile of the signal along the spacecraft trajectory near
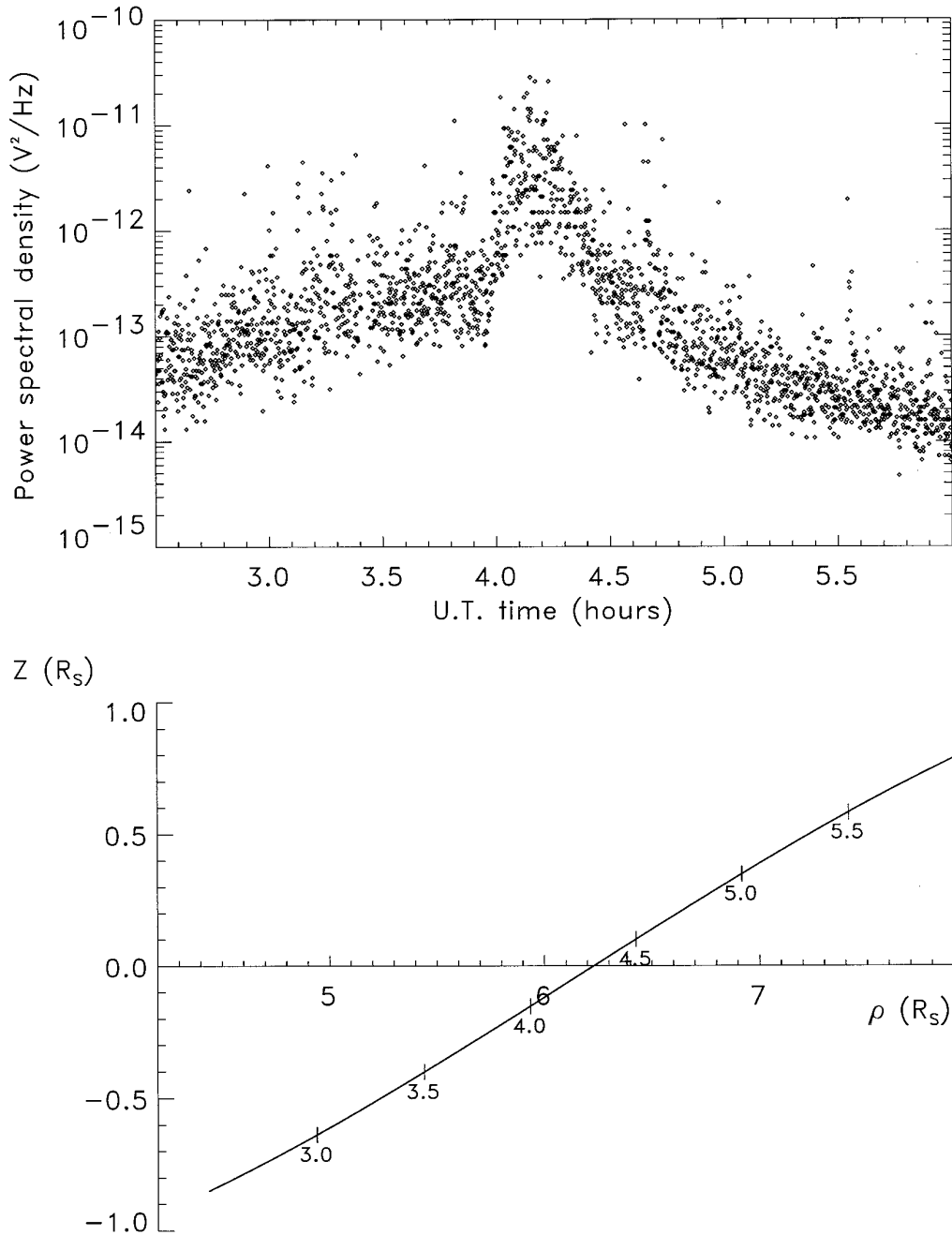
FIG. 2.   Upper panel: Voltage power spectral density V_0^2 in the PRA 20.4 kHz channel as a function of time (in decimal hours). Lower panel: Sketch of the spacecraft trajectory projected in a meridian plane of Saturn; z is the distance from the equator and ρ the distance from Saturn's spin axis (both in Saturn's radii R_S). The time is plotted on the trajectory every 0.5 hr.

the ring plane will be used to infer the grain spatial distribution.

Figure 5 summarizes our observations: the upper panel shows the power spectral density in the 20.4 kHz channel as a function of time and vertical distance. The lower panel shows the power spectrum at several spacecraft positions as indicated.

3. THEORETICAL SPECTRUM FROM DUST AND PLASMA IMPACTS

3.1. Grain Impact Ionization

When a dust grain impacts a solid target at a velocity larger than a few km/sec, it undergoes a strong shock compression which vaporizes and ionizes it (as also a part of
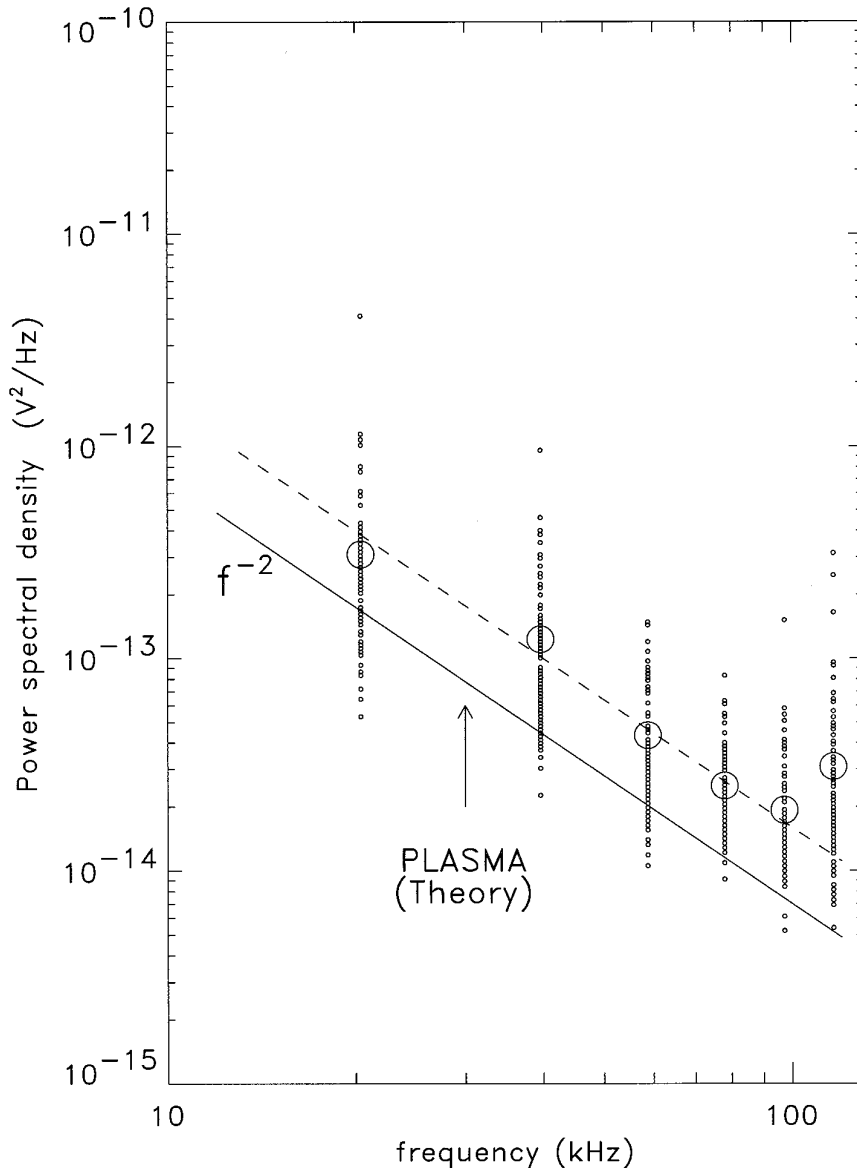
FIG. 3. Voltage power spectrum near 3.6 hr. We have plotted all the PRA measurements (dots) during a 12 min interval centered at this time, the corresponding average spectrum (big circles), and the best f^{-2} line (dashed). The continuous line shows the maximum value of the theoretical (f^{-2}) spectrum produced by impacts of ambient plasma particles or photoelectron emission, calculated in Section 3.3.

the target material). This material then expands into the low-pressure ambient medium, cooling and partially recombining (Drapatz and Michel 1974). The residual ionization of the expanding plasma cloudlet can be used to detect the grain: in practice, one measures the charge Q carried by the ions (or the electrons) by separating them and recollecting one species; the grain mass m is then deduced from laboratory calibrations of the relation $Q(m)$. This is the principle of impact ionization detectors (see Fechtig *et al.* 1978).

The charge Q varies more strongly with the impact velocity v_G than a simple proportionality to the kinetic energy mv_G^2. Instead,

$$Q \propto m^\alpha v_G^\beta \qquad (3)$$

with $2.5 < \beta < 4$ and $0.7 \leq \alpha \leq 1$; α is expected to be smaller than one when recombination and surface phenomena play an important role, which should occur for very large grains (see Krüger and Kissel 1984).

To infer the relation $Q(m)$, we use extensive laboratory measurements carried out to calibrate the dust detectors for the missions Giotto (Göller *et al.* 1986), Galileo, and Ulysses (Göller and Grün 1989). The charge Q was found to be proportional to the grain mass m in the range $10^{-15} < m < 10^{-10}$ g, and the coefficient of proportionality was measured in a large range of velocities.
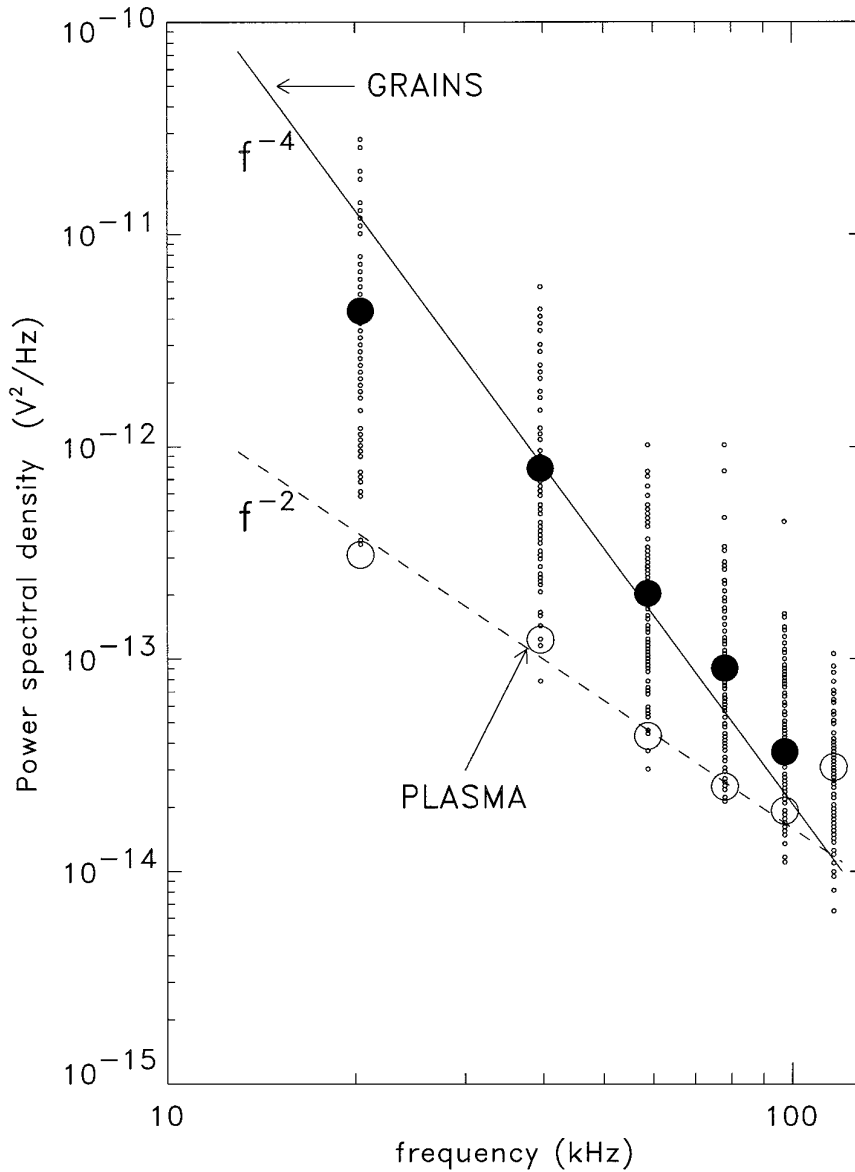
FIG. 4. Voltage power spectrum near 4.2 hr. We have plotted all the PRA measurements (dots) during a 12 min interval centered at this time. The corresponding average spectrum minus the mean spectrum due to plasma effects (big circles, cf. Fig. 3) is plotted as big black dots. The heavy line shows the theoretical (f^{-4}) spectrum produced by dust grains of radius such that $(\langle r^6 \rangle)^{1/6} \approx 1.2$ μm and concentration 3.6×10^{-3} m^{-3}, as calculated in Sections 3 and 4.

The velocity of dust grains in circular Keplerian orbits at $R \approx 6.1$ R_S from Saturn is $(M_S G/R)^{1/2} = 10.1$ km/sec. Since the grain orbital eccentricities are not well known, we consider particles on equatorial (prograde) circular orbits; we will discuss in Section 6 the effect of nonzero eccentricities. With the spacecraft velocity given in Section 2, we deduce the grain velocity in the spacecraft frame:

$$v_G = 18.5 \text{ km/sec}$$

(mainly due to the spacecraft radial velocity with respect to Saturn). With this value of v_G, the laboratory measurements give approximately $Q/m \approx 0.5$–2 Cb/g for carbon, silicate, and iron particles impinging on a gold-plated target (Göller and Grün 1989), $Q/m \approx 2$ and 10 Cb/g for impacts of iron particles on, respectively, aluminium and gold (Grün 1984), and $Q/m \approx 3$–15 or 2–8 Cb/g for, respectively, silicate (Göller et al. 1986) or iron (Grün et al. 1984) particles on a gold target. These values were generally found to be weakly dependent of the impact angle.

For impacts of E ring grains on the Voyager spacecraft body and the antennae, the ratio Q/m is not easy to assess
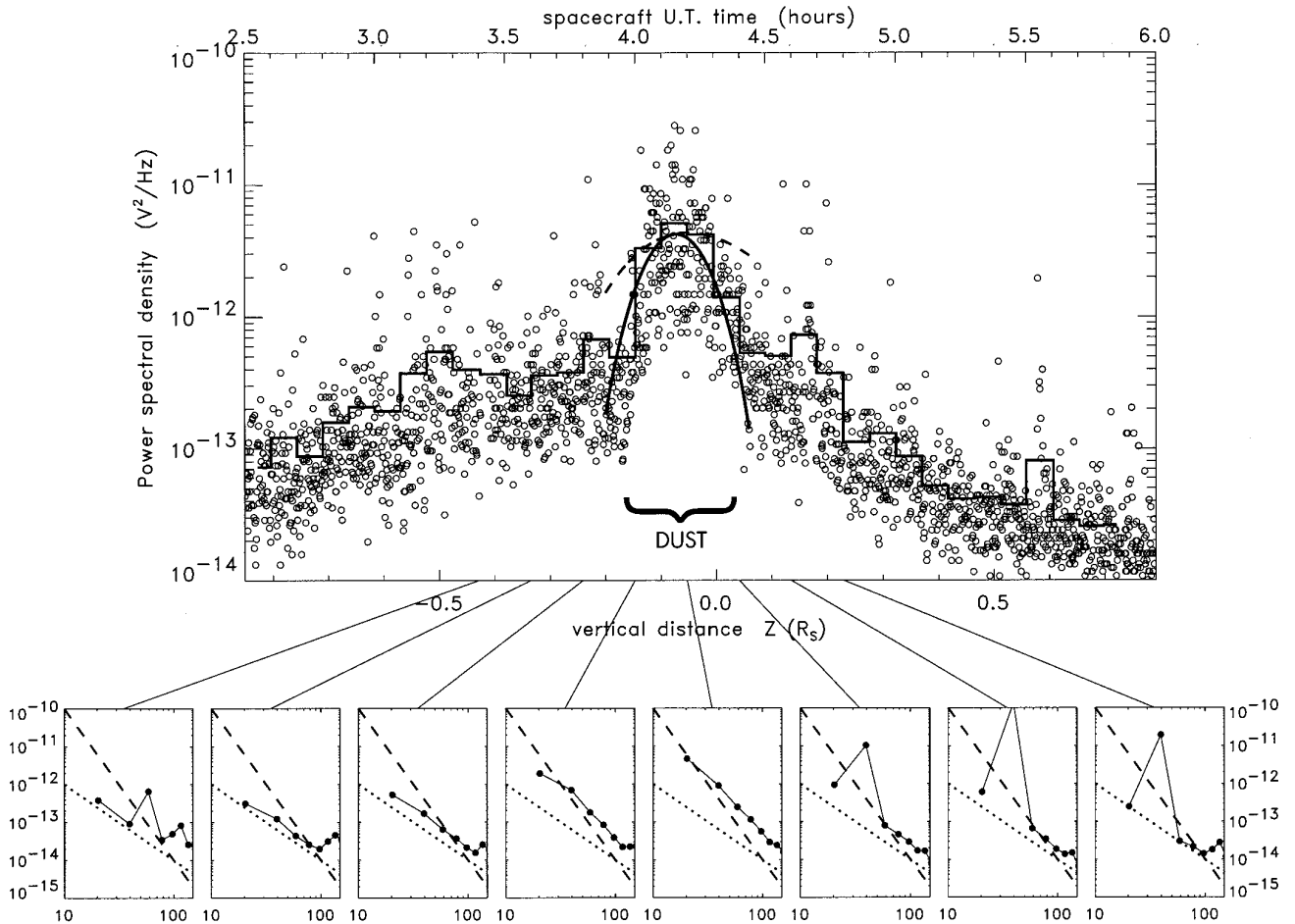
FIG. 5. Upper panel: Voltage power spectral density in the 20.4 kHz channel as a function of vertical distance and time. We have plotted individual measurements (small circles), and their average in bins of 0.1 hr. The dashed curve is the theoretical level produced by dust grains of mean radius 1 μm (as determined in Section 4.2) with the concentration given by the model of Showalter *et al.* (1991), as calculated in Sections 3 and 4. The continuous curve is obtained with the same model, but assuming that the grain size decreases with vertical distance from our maximum, by about 10% over 4000 km (cf. Fig. 7). Lower panel: Power spectrum at the locations indicated (V_0^2 in V^2 Hz^{-1}, f in kHz); for comparison we have drawn a f^{-4} spectrum (dashed) and a f^{-2} spectrum (dotted).

since little is known about the state and composition of the particles, and the surface exposed to impacts is made of different materials of unknown yields. The large telemetry antenna, which represents most of the surface, is made of a material expected to have a very low yield to dust impacts. On the other hand, the metallic part of the spacecraft and the PRA antennae have a total projected surface of order of magnitude 1 m^2, whereas the rest of the spacecraft is expected to have a low (unknown) yield.

Hence, as a conservative estimate, we will assume

$$Q/m \approx 2 \ \text{Cb/g} \qquad (4)$$

(on the order of the laboratory measurements for metallic targets), over a total projected surface of

$$S \approx 1 \ \text{m}^2$$

(on the order of the total projected surface made of metallic material).

Note that for icy grains of radius 1 μm, the yield given in (4) is nearly twice larger than the value taken by Meyer-Vernet *et al.* (1986a) scaled to the proper velocity. Likewise, substituting (4) into (3) with $\alpha = 1$ and $\beta \approx 3.5$ (which is roughly the mean exponent in the velocity range 10–30 km/sec), we obtain $Q/m \approx 7 \times 10^{-5} v_G^{3.5}$ Cb/g, which is also nearly twice larger than the value taken by Pedersen *et al.* (1991), who used an average over the surfaces exposed. This difference is within the estimated uncertainties, and anyway, the product $(Q/m)\sqrt{S}$, which is the relevant quantity for deducing the grain mass (see Section 3.2), is roughly the same as in these papers.

For icy grains of radius r_μ (in micrometers), Eq. (4) yields

$$Q \approx 0.8 \times 10^{-11} \times r_\mu^3 \ \text{Cb} \qquad (5)$$

For a micrometer-sized particle, this corresponds to 5×10^7 electron charges, which is about 10^4 times more than the electrostatic charge normally carried by such a grain in this environment (see Horanyi et al. 1992).

3.2. Voltage Spectrum Produced by Dust Impacts

In conventional dust detectors, the charge Q released by the impacts is collected by a biased plate. In the case of PRA, it is collected by the conductive structure of the spacecraft, producing a time variation of the voltage detected by the instrument.

The amplitude of the signal produced on a PRA monopole by one grain impact is

$$V_{max} \approx Q/C,$$

C being the spacecraft capacitance, estimated from rheographic measurements (R. Manning, personal communication 1994) to be roughly

$$C \approx 300 \text{ pF}.$$

We approximate the signal $V(t)$ produced by a particle impact as increasing to V_{max} with the rise time τ_r, and decaying with the time constant $\tau_d \gg \tau_r$. At frequencies $f \gg 1/2\pi\tau_r$, the Fourier transform is determined by the discontinuity of the derivative in the rising part (see Meyer-Vernet 1985) and is given by

$$\begin{aligned}|V(\omega)| &= V_{max}/\tau_r\omega^2 \\ &= Q/C\tau_r\omega^2.\end{aligned} \qquad (6)$$

The time scale τ_r can be evaluated as in (Meyer-Vernet et al. 1986a) from elementary physical constraints. First, the cloud may be approximated as expanding radially with a velocity $v_{ex} \sim v_G/(1 + \sqrt{A})$, A being the grain-to-target specific density ratio (Drapatz and Michel 1974). This gives $v_{ex} \sim 10$ km/sec. The signal rise time τ_r must be smaller than the time taken by the cloud's diameter ($2v_{ex}t$) to reach the spacecraft typical size $D \sim 1$ m, i.e.,

$$\tau_r < D/2v_{ex} \sim 5 \times 10^{-5} \text{ sec}.$$

Second, τ_r must be smaller than the time taken by the plasma density in the cloud

$$n_C \sim \frac{Q/e}{4\pi(v_{ex}t)^3/3}$$

to decrease to the ambient level n. Near the equator at distance $R \approx 6.1 \ R_S$, $n \approx 25$ cm^{-3} (Richardson and Sittler 1990). Hence,

$$\tau_r < (3Q/4\pi ne)^{1/3}/v_{ex} \sim 8 \times 10^{-5} \times r_\mu \text{ sec},$$

where we have substituted the expression of Q given in (5). Thirdly, τ_r is probably larger than (or equal to a significant fraction of) the time taken by the cloud radius ($v_{ex}t$) to become smaller than its proper Debye length ($(\varepsilon_0 KT_C/n_Ce^2)^{1/2} \propto t^{3/2}$), in order to allow charge separation in the cloud. This yields

$$\tau_r \geq \frac{3Qe}{4\pi\varepsilon_0 v_{ex}KT_C} \sim 2 \times 10^{-5} \times r_\mu^3 \text{ sec},$$

where we have substituted the expression of Q given in (5) and assumed for the temperature of the coldest species in the cloud (which determines the Debye length) $T_C \sim 1$ eV (Hornung and Drapatz 1981).

We get a final constraint from the PWS instrument. The waveform observations (Gurnett et al. 1983) indicate a signal rise time roughly equal to the time resolution of the instrument which is about 30 μsec, so that $\tau_r < 3 \times 10^{-5}$ sec. This holds for all the other planetary encounters; for the present one no waveform data were available, and hence this latter constraint must be used with caution (see also Section 5).

All in all, it seems reasonable to assume for $r \approx 1 \ \mu$m grains

$$\tau_r \sim 2 \times 10^{-5} \text{ sec}$$

as in (Meyer-Vernet et al. 1986a) and (Pedersen et al. 1991). Incidentally, we note that despite the difference in experimental setup, this is in the range of the values measured for the dust detectors at the impact velocity v_G (Fechtig et al. 1978, Göller and Grün 1989).

We can now deduce the voltage power spectral density produced by N (uncorrelated) particle impacts per second

$$V^2 = 2N|V(\omega)|^2. \qquad (7)$$

Substituting the expression (6) of $|V(\omega)|$ with the parameters determined above, we get

$$V^2 \sim 2.3 \times 10^3 Nr_\mu^6/f^4. \qquad (8)$$

The impact rate can be expressed as a function of the grain number density n_G as

$$N = n_G v_G S \sim 1.8 \times 10^4 n_G. \qquad (9)$$

Substituting this value in (8) and using the calibration (2), we deduce the theoretical level

$$V_0^2 \sim 1.7 \times 10^8 n_G r^6/f^4 \qquad (10)$$

(V_0^2 in V^2Hz^{-1}, n_G in m^{-3}, f in Hz). To simplify the notation, from now on r stands for r_μ, the grain radius in micrometers. When the grains have a size distribution of nonzero width, this should be written as

$$V_0^2 \sim 1.7 \times 10^8 n_G \langle r^6 \rangle / f^4 \quad \text{(grain impacts)} \quad (11)$$

for $f > 2 \times 10^5$ Hz, where the brackets stand for a mean over the size distribution.

3.3. Plasma Contribution

Let us now calculate the noise produced by the ambient plasma in absence of instabilities. This will give a minimum level, since if the plasma is unstable the noise is expected to be larger. This (stable) plasma noise has two components:

—the thermal noise produced by the (quasi)-thermal motion of the ambient plasma particles, which induces electrostatic voltage pulses on the antennae, and

—the shot noise produced by the plasma particles impacting the conductive structure of the spacecraft or of the antennae.

Near the equator crossing, the density and temperature of the ambient electrons are $n \approx 25$ cm^{-3} and $T \approx 10^5$ K (Richardson and Sittler 1990); the corresponding electron plasma frequency and Debye length are $f_p \approx 45$ kHz and $L_D \approx 4$ m. With a PRA monopole of length $L = 10$ m, the quasi-thermal noise for $f < f_p$ is (Meyer-Vernet and Perche 1989)

$$V_{QT}^2 \approx 0.6 \times 10^{-14} \text{ V}^2\text{Hz}^{-1} \quad (12)$$

with a peak at $f \approx f_p$ where the noise increases by roughly the ratio T_h/T_c of the hot and cold electron temperatures. With $T_h/T_c \approx 10$ (Richardson and Sittler 1990), this gives

$$V_{QT}^2 \approx 0.6 \times 10^{-13} \text{ V}^2\text{Hz}^{-1} \quad \text{for } f \approx f_p \approx 45 \text{ kHz.} \quad (13)$$

For $f > f_p$, the noise decreases below the level (12).

A comparison with the spectra plotted in Fig. 5 shows that the plasma quasi-thermal noise is negligible compared to the observed spectral density. Although the plasma frequency peak is often observed near 40 kHz, its level is much larger than the value (13) and exhibits large fluctuations; this strongly suggests a plasma instability.

Let us now calculate the shot noise produced by the plasma particles impacting the spacecraft (or the antennae), or by the photoelectrons emitted by their surfaces. The corresponding spectral density on a PRA monopole is (Meyer-Vernet and Perche 1989)

$$V_I^2 \approx 2N_P e^2/(C\omega)^2, \quad (14)$$

where the number of plasma particle impacts per second is roughly

$$N_P \approx 2n \left(\frac{KT}{2\pi m_e} \right)^{1/2} S_P \quad (15)$$

when the spacecraft floating electrostatic potential is smaller in modulus than KT/e, so that it does not modify the electron trajectories very much. Here, S_P is the equivalent collecting surface of the *whole conductive structure* of the spacecraft and antennae. If the spacecraft potential Φ is negative and not small with respect to KT/e, the plasma electrons are repelled, so that the shot noise is smaller. Since Φ was negative near equator crossing (but not precisely measured) (Richardson and Sittler 1990), we thus consider the above expression as an upper limit. With $S_P \sim 50$ m^2 and the plasma parameters encountered near the equator crossing, Eqs. (14) and (15) give

$$V_0^2 \lesssim 0.7 \times 10^{-4}/f^2 V^2 H_2^{-1} \quad \text{(plasma impacts).} \quad (16)$$

As previously, we have used the calibration (2) since, as for grain impacts, the relevant capacitance is that of the spacecraft. Farther from the equator, the theoretical spectrum becomes smaller since the plasma density decreases, but it remains on the same order of magnitude in the region analyzed in this paper, which is within one density scale height (~ 1 R_S) from equator. Note that the value calculated by (Aubier *et al.* 1983) was much larger because the relevant capacitance was incorrectly estimated.

Equation (16) is drawn on Fig. 3. One sees that this level—which is a maximum level—is about twice smaller than the observed mean spectral density. Note also that the number of electron impacts per individual measurement of duration $\delta t = 0.025$ sec is of order $N_P \delta t \sim 10^{13}$, which is a very large number. Thus, except in presence of large fluctuations of the plasma parameters, the plasma shot noise should not exhibit large amplitude fluctuations, contrary to what is observed. We thus conclude that the plasma shot noise can only be responsible for a part of the voltage observed in the broad structure surrounding the ring plane. We attribute the remaining part to plasma instabilities, which might also explain the large dispersion of the data. These instabilities are not expected to be related to the dust since the dust-plasma streaming instability occurs at very low frequencies (see, for example, Havnes, 1988).

4. INFERRING DUST PROPERTIES

We shall now infer the dust parameters from the data showing the narrow hump around the ring plane (within the time period 4.0–4.4 hr), where the noise is mainly produced by grain impacts.

4.1. Dust Parameters at the Location where the Signal is Maximum

To infer the dust parameters at the location of the maximum of the hump near 4.2 hr ($R \approx 6.1\ R_S$, $z \approx -0.08\ R_S$), we will first use the data plotted in Fig. 4. The best fitted f^{-4} spectrum is

$$V_0^2 \approx 2 \times 10^6/f^4\ \text{V}^2\text{Hz}^{-1}. \qquad (17)$$

Comparing with the theoretical level (11) produced by a number density n_G of dust grains having radius r, we find

$$n_G\langle r^6 \rangle \sim 1.2 \times 10^{-2}\ \text{m}^{-3} \times \mu^6. \qquad (18)$$

This result alone is not sufficient to determine independently the particle concentration and size. Furthermore, the numerical value in Eq. (18) is proportional to the factor $[C\tau_r/(Q/m)]^2/S$ which is not accurately known, and the level (17) takes into account the highest frequencies which may be polluted by the plasma noise. Fortunately, since $V_0^2 \propto n_G\langle r^6 \rangle$, our measurement is much more sensitive to the grain size than to the other parameters. Hence we will assume that the concentration is equal to that given by the optical model (Showalter *et al.* 1991), and then deduce the grain size. An error either in n_G, in the above factor, or in the level (17) should translate into a much smaller error in the radius. We will return to this point in Section 6.

This optical model gives for grains of radius $r \approx 1\ \mu$m at Enceladus orbit ($R_{\text{ENC}} = 3.94\ R_S$)

$$\int_{-\infty}^{+\infty} dz\, n_G(R, z)$$

$$\approx 1.8 \times 10^6\ \text{particles/m}^2 \quad \text{for } R = R_{\text{ENC}} \qquad (19)$$

$$\propto (R_{\text{ENC}}/R)^7 \qquad\qquad \text{for } R > R_{\text{ENC}}. \qquad (20)$$

In this model, the concentration varies with the distance z from equator as

$$n_G \propto e^{-z^2/2\sigma^2}, \qquad (21)$$

where σ increases with the distance R from Saturn as

$$\sigma(R) \propto 6.3^{R/5} \qquad (22)$$

with

$$\sigma \approx 0.13\ R_S \approx 7.9 \times 10^6\ \text{m} \quad \text{for } R \approx 6.1\ R_S. \qquad (23)$$

Hence, writing

$$\int_{-\infty}^{+\infty} dz\, n_G(R, z)$$

$$\approx n_G(R, 0) \times \sigma(R)\sqrt{2\pi} \qquad (24)$$

$$\approx 1.8 \times 10^6 \times (3.94/6.1)^7 \quad \text{for } R \approx 6.1\ R_S \qquad (25)$$

we deduce $n_G(6.1\ R_S, 0) \approx 4.3 \times 10^{-3}\ \text{m}^{-3}$, which gives

$$n_G \approx 3.6 \times 10^{-3}\ \text{m}^{-3} \quad \text{at } z \approx -0.08\ R_S, R \approx 6.1\ R_S. \qquad (26)$$

Substituting in (18), we get

$$[\langle r^6 \rangle]^{1/6} \approx 1.2\ \mu\text{m}. \qquad (27)$$

This value is close to the mean radius $\langle r \rangle = (1.0 \pm 0.3)$ μm given by the optical model (Showalter *et al.* 1991). However, in order to deduce $\langle r \rangle$ from the moment of order 6 determined above, we must know the width of the grain size distribution.

4.2. Grain Size Distribution at the Location Where the Signal is Maximum

To estimate this size distribution, we will use the scatter of the data in the 20.4 kHz channel (where the levels are much larger than the plasma noise).

We have plotted in Fig. 6 the histogram of the voltage power spectral densities V_0^2 measured at 20.4 kHz during the 12 min interval surrounding our peak at 4.2 hr. Each data point V_0^2 represents an individual measurement of duration $\delta t = 0.025$ sec. The histogram shows the proportion of points (in a total of 120) in each bin of size $\Delta[\log V_0^2] = 0.2$.

The width of the histogram is produced by two main effects:

—the fluctuations in the size of the impacting grain(s), due to the nonzero width of the size distribution, and

—the fluctuations in the number of dust impacts during an individual measurement (plus a contribution of the plasma noise which is only significant for very low signals, i.e., in the extreme left wing of the histogram, near the levels shown in Fig. 3 for 20.4 kHz).

With a grain concentration of $n_G \approx 3.6 \times 10^{-3}\ \text{m}^{-3}$, the mean impact rate is, from (9), $N \approx 65\ \text{sec}^{-1}$, so that the mean number of impacts during an individual measurement of duration δt is

$$N_{\delta t} \approx 65 \times \delta t = 1.6.$$

Assuming Poisson statistics, the probability to have k impacts during δt is

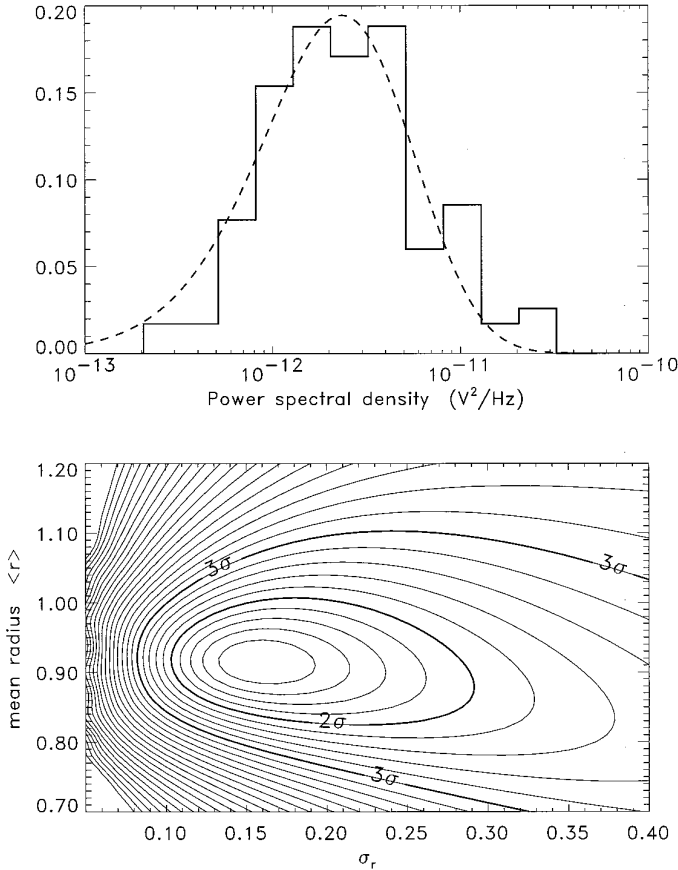$$P(k) = e^{-1.6}(1.6)^k/k!. \qquad (28)$$

FIG. 6. The upper panel shows the histogram of the data in the 20.4 kHz channel (proportion of the data in bins of $\Delta [\log V_0^2] = 0.2$ as a function of V_0^2). The dashed curve is the theoretical histogram produced by a Gaussian grain size distribution of mean radius 0.91 μm and fractional dispersion 0.16, calculated in Section 4.2 with a simplified model. The lower panel shows labelled isocontours of the standard deviation between the model and the observations (here, σ denotes the minimum value given by the mean-square fitting).

We deduce that the most frequent events are one or two impacts during an individual measurement ($P(1) = 0.32$, $P(2) = 0.26$). If the particles were all of the same size, the histogram would consist of discrete (zero-width) peaks at multiples of the level corresponding to one impact, plus a left-hand side wing around 3×10^{-13} V^2 Hz^{-1} produced by the plasma noise. Since this is obviously not the case, we expect the width of the grain size distribution to contribute significantly. In particular, since a grain of radius r contributes as $V_0^2 \propto r^6$, the smoothing out of the discretization between one or two impacts suggests that the relative (full) width of the size distribution is at least on the order of magnitude of $2^{1/6} - 1 \sim 0.1$.

Let us take a Gaussian distribution centered on the mean radius $\langle r \rangle$:

$$n_G(r) = \frac{n_G}{\sigma_r \langle r \rangle \sqrt{2\pi}} e^{-(r/\langle r \rangle - 1)^2/2\sigma_r^2}, \qquad (29)$$

where $n_G(r) \, dr$ is the number density of grains of radius within an interval dr around r (in micrometers), and the fractional size dispersion

$$\sqrt{\langle (r/\langle r \rangle - 1)^2 \rangle} = \sigma_r$$

is assumed to be much smaller than one. To simplify the analysis, we calculate the theoretical voltage histogram as if $N_{\delta t}$ grain, with given radius r obeying the distribution (29), did impact during each individual measurement (δt). For such an approximation to be acceptable, two conditions are necessary: (i) $N_{\delta t}$ must be about one (which is true), and (ii) the shape of the histogram must be mainly produced by the size distribution, i.e., the relative full width at half-maximum ($\approx 2.35 \, \sigma_r$) must be significantly larger than the value 0.1 estimated above (which will be justified *a posteriori*). The proportion of data points in a bin of size $\Delta [\log V_0^2] = 0.2$ is then equal to the proportion of impacting grains of radius within an interval Δr around r, with r and Δr deduced from Eq. (10) with $f = 20.4 \times 10^3$ Hz and $n_G = 3.6 \times 10^{-3}$ m^{-3} (equivalent to $N_{\delta t} \approx 1.6$):

$$r = [2.8 \times 10^{11} \times V_0^2]^{1/6}$$

$$\Delta r/r = \ln 10 \times (\Delta V_0^2/V_0^2)/6 = 0.077.$$

This gives the theoretical histogram

$$H = \frac{0.077}{\sigma_r \langle r \rangle \sqrt{2\pi}} (2.8 \times 10^{11} \times V_0^2)^{1/6}$$
$$\exp - [(2.8 \times 10^{11} \times V_0^2)^{1/6}/\langle r \rangle - 1]^2/2\sigma_r^2. \qquad (30)$$

A mean-square fitting of this expression to the observed histogram gives the following mean and variance of the distribution

$$\langle r \rangle \approx 0.91 \ \mu\text{m} \pm 0.1 \quad (2\sigma) \quad \text{(value deduced from}$$
$$\text{the histogram)} \qquad (31)$$
$$\sigma_r \approx 0.16 \pm^{0.13}_{0.06} \qquad (2\sigma).$$

With $\sigma_r \approx 0.1$–0.3, the grain size distribution has a full (relative) width at half maximum of 0.2–0.7, which satisfies condition (ii) above. We have drawn Eq. (30) with these parameters in Fig. 6. The accuracy of this determination of $\langle r \rangle$ and σ_r is indicated by the isocontours of standard deviation between the model and the observations, in a $[\langle r \rangle, \sigma_r]$ plane (lower panel of Fig. 6).

The agreement between the observed and calculated histograms is rather good, keeping in mind that the fitting was done with only two free parameters. Note that the fitting could not be expected to be better owing to the crudeness of our model; in particular, the plateau-like shape observed at the top of the histogram may be attrib-

uted to the discretization of the impacts, the most frequent cases being one or two impacts per individual measurement. As a consequence, the uncertainties in our determination of both the mean radius $\langle r \rangle$ and the variance σ_r might be larger than those determined from the accuracy of the fitting.

Let us now compare the mean radius $\langle r \rangle$ given by the fitting with that obtained in Section 4.1. With $\sigma_r \approx 0.1$–0.3, we have

$$[\langle r^6 \rangle]^{1/6}/\langle r \rangle \approx 1.0\text{–}1.2 \tag{32}$$

so that the value of $[\langle r^6 \rangle]^{1/6} \approx 1.2\ \mu m$ found in Section 4.1 is equivalent to

$$\langle r \rangle \approx 1.0\text{–}1.2\ \mu m \quad \text{(value deduced from the mean spectrum).}$$

The rough agreement between this value and the one determined from the histogram is an indication of the degree of consistency of the results. (Note in particular that the histogram deals with the levels in the channel 20.4 kHz, whereas in Section 4.1 we used the mean over five channels (normalized to f^{-4} and with plasma noise tentatively substracted).) Hence our best estimate is

$$\langle r \rangle \approx 1.0\ \mu m. \tag{33}$$

Let us now make a comparison with the optical model. Showalter *et al.* (1991) use a distribution of the form

$$n_G(r) \propto \left(\frac{r}{\langle r \rangle} \right)^{1/\sigma_r^2} e^{-(r/\langle r \rangle - 1)/\sigma_r^2}$$

with $\langle r \rangle \approx 1.0\ \mu m$ and $\sigma_r \approx 0.3$. Although this distribution is not Gaussian, σ_r has a similar meaning (provided it is small) since it represents the variance, whereas the full (relative) width at half-maximum is also given by $2\sigma_r\sqrt{2 \ln 2}$.

Thus, we find roughly the same mean radius and distribution width as the optical model. Note, however, that our measurement is local, whereas the optical model is based on measurements involving a line-of-sight integration.

4.3. Spatial Distribution

Let us now compare the variation of the signal V_0^2 observed along the spacecraft trajectory around the ring plane, to the grain spatial distribution given by the optical
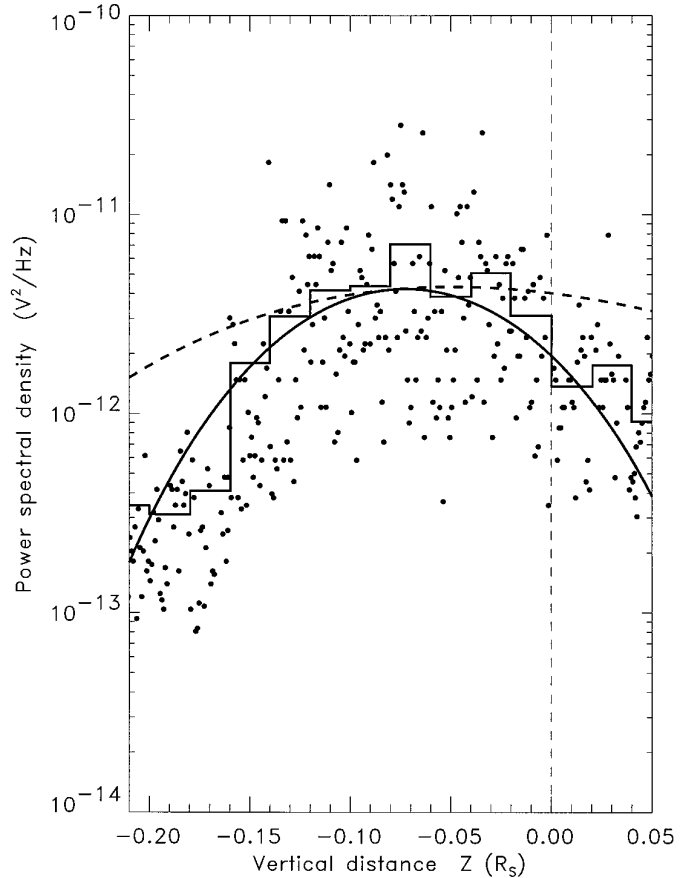

FIG. 7. Voltage power spectral density V_0^2 at 20.4 kHz, as a function of vertical distance. We have plotted individual measurements and their average in bins of 0.02 hr. The dashed curve is the theoretical level produced by dust grains of mean radius 1 μm with the concentration given by the model of Showalter *et al.* (1991), as calculated in Sections 3 and 4. The heavy curve is obtained with the same model, but assuming that the grain size decreases with vertical distance from our maximum, by about 10% over 4000 km.

model. The observations are plotted in Fig. 7, showing the data in the 20.4 kHz channel as a function of the distance from the ring plane. The profile has a maximum southward of equator, at $z = z_0 \approx -0.08(\pm 0.03)\ R_S$, and its full vertical width at half-maximum is about 0.13 R_S.

To calculate the theoretical V_0^2 profile expected from the model of Showalter *et al.* (1991), we first assume, as these authors did, that the grain size distribution does not vary within the ring. In this case, V_0^2 should vary proportional to the particle concentration n_G, which is defined in Eqs. (20)–(25). The factor of proportionality is deduced from Eq. (11) with the mean grain radius $\langle r \rangle \approx 1\ \mu m$ determined in Section 4.2 (and σ_r from Eq. (31)).

The resulting profile is drawn in Fig. 7 (dashed curve). It has a maximum slightly southward of the equator, albeit

closer to the equator than observed, and is not symmetrical. This lack of symmetry is due to the increasing distance from Saturn (i.e., the decreasing grain concentration at equator) during the ring plane crossing. The full width at half-maximum in vertical distance ($2\sigma\sqrt{2 \ln 2}$ with σ given in (22)–(23)) is about 0.3 R_S, which is 2.3 times more than observed. As there is no reason for the grain size distribution to be uniform within the ring, a possible explanation of this discrepancy is that the mean grain size decreases with vertical distance. Since $V_0^2 \propto \langle r^6 \rangle$, a small decrease in grain radius yields a large decrease in V_0^2. To illustrate this point, we have plotted in Fig. 7 (continuous curve) the theoretical profile calculated with the following simple assumptions:

—$n_G(R, z)$ still given by the model of Showalter et al. (1991),
—particle mean radius decreasing with vertical distance from z_0, as

$$\langle r \rangle \propto 1 - (z - z_0)^2/3\sigma^2 \quad \text{(for } |z - z_0| \leq \sigma \approx 0.13), \quad (34)$$

where the distances are in units of Saturn's radius $R_S \approx$ 60,330 km. This fits rather well the measured profile. It is important to note, however, that our data are not sufficient to determine accurately the variation of $\langle r \rangle$ with z. Other functions decreasing similarly with z might satisfy the observations equally well. Another possibility is that the yield Q/m might decrease with vertical distance, for example, due to a decrease in grain velocity with respect to the spacecraft; we shall return to this point in the discussion in Section 6.

5. REMARKS ON THE PLASMA WAVE INSTRUMENT

Let us now try to compare our results with the diagnostics of the E ring made recently from the data of the Plasma Wave instrument (PWS) aboard Voyager 1 (Tsintikidis et al. 1995). As shown in Section 3.3, we agree with these authors claiming that the voltage observed close to the ring plane is not produced by the plasma shot noise. The vertical profiles derived from both instruments are difficult to compare since they do not concern the same physical quantity. The full width at half-maximum deduced from PWS (which is argued to concern the grain concentration profile n_G) is twice smaller than the PRA result (which concerns the $n_G r^6$ profile and is thus highly ponderated by the grain radius). Likewise, PWS finds a maximum closer to equator than PRA.

On the other hand, PRA and PWS disagree on the grain size. For icy particles, the background level of the observed PWS spectrum is argued to correspond to grains of radius 5 μm. To get the same result, PRA should have measured a power spectrum 1.5×10^4 times larger than observed,

or our analysis above must use a value of the parameter $[C\tau_r/(Q/m)]^2/S$ larger by the same factor. This is much larger than our uncertainties.

However, as already noted, the PRA instrument uses a monopole configuration; i.e., it measures the voltage between one antenna arm and the spacecraft. On the other hand, the PWS instrument is operated as an electric dipole; i.e., it measures the difference of potential between the two antenna arms. Hence, not only does it respond very weakly to dust impacts on the spacecraft, but its response is unknown, since it depends on the dissymmetry of the system.

Hence the *monopole* configuration is more adequate to detect dust impacts on the spacecraft (Meyer-Vernet et al. 1986b; see also Oberc 1994). Since 1986 the PWS investigators have deduced grain parameters by calibrating their results on the PRA levels (Gurnett et al. 1987, 1989, Tsintikidis et al. 1994, 1995). Tsintikidis et al. (1994, 1995) have introduced a mean calibration of the PWS instrument, based on the observed PRA power spectra for several planetary encounters. However, except for the Uranus encounter where the PWS calibration was indeed in agreement with the published PRA levels, all the other PWS calibrations were in fact based on incorrect PRA power spectra, offset from the true PRA spectra by factors ranging from 4^2 to 15^2 for V_0^2.

Another problem is that Tsintikidis et al. (1995) state that the relative velocity between the spacecraft and the dust is 29.3 km/sec for grains in prograde circular orbits, whereas the actual value is 18.5 km/sec. Since the power spectrum varies as $V^2 \propto NQ^2 \propto v^8$, this should produce an erroneous factor of $(29.3/18.5)^8 \approx 40$. However, the above authors nevertheless find a yield Q/m corresponding to the correct velocity, so that the error in velocity only changes the relation between the impact rate N and the grain concentration.

6. SUMMARY AND DISCUSSION

We summarize below the results of the PRA measurements acquired when Voyager 1 crossed the E ring near 6.1 R_S from Saturn.

—From the data acquired when the signal was maximum, we have inferred that the grain mean radius at this location is $\langle r \rangle \approx 1$ μm. This result has been obtained with two different methods, both using the particle concentration given by the model of Showalter et al. (1991). The determination depends (at the power $\frac{1}{6}$) on the assumed grain concentration, and on the parameter $[C\tau_r/(Q/m)]^2/S$ which is poorly known. This parameter might be off by a factor that we estimate to be at most 10^2, but even with such a large error, the resulting error in the mean radius would only be a factor of two.

—From the data histogram at the above location, we

have found that the fractional dispersion of the grain size distribution is $\sigma_r \approx 0.1$–0.3. Even though our results are local, they confirm the narrow grain size distribution obtained from the optical data (Showalter *et al.* 1991), and first suggested by Pang *et al.* (1984).

—The variation of the PRA signal observed along the spacecraft trajectory through the E ring gives a thickness 2.3 times less than that of the optical model, if the grain size distribution is assumed constant within the region explored. This discrepancy can be explained by instead assuming that the mean grain size decreases with vertical distance, by about 10% over 4000 km. Indeed, the grain size has no reason to remain constant within the E ring (see Horanyi *et al.* 1992, Hamilton 1993, Hamilton and Burns 1994).

—Finally, the maximum of the PRA signal is offset with respect to the ring plane, by 0.08 ± 0.03 R_S southward, which is larger than the value expected from the increasing distance from Saturn during the encounter. This result is not very surprising in view of the (time dependent) vertical dissymmetry predicted by theoretical models (see Horanyi *et al.* 1992, Hamilton and Burns 1994). Unfortunately, our data are not sufficient to decide whether this dissymmetry concerns the concentration or the size (or velocity) of the dust grains.

These results were obtained by assuming conservatively that the grains move on circular (prograde) orbits. In this case, the Keplerian velocity $v_K = 10.1$ km/sec roughly cancels the spacecraft azimuthal velocity, yielding a grain impact velocity of $v_G = 18.5$ km/sec (mainly due to the spacecraft radial velocity with respect to Saturn). However, the E ring particles are thought to move on eccentric orbits, with a small inclination (Horanyi *et al.* 1992), so that the impact velocities may be different from the above value. We examine below how the corresponding change in the yield Q/m might change our results. Since the orbital eccentricity may be related to the grain size and location, the problem is in general very complicated, and we only give some rough estimates.

Since v_G is mainly radial, the change produced by an eccentricity $e \neq 0$ is mainly due to the grain radial velocity, which is at most of order of magnitude ev_K; this yields a relative change in v_G smaller than about ev_K/v_G (positive or negative depending on the position on the orbit). With the above values of v_K and v_G, the maximum relative change is $\Delta v_G/v_G \sim 0.5e$. Since grains of radius r and impact velocity v_G contribute to the observed PRA level as $V_0^2 \propto r^6 v_G^{2\beta+1}$ with $\beta \approx 3.5$, $\Delta v_G/v_G \sim 0.5e$ is equivalent to a relative change in radius $\Delta r/r \sim 0.7e$.

Hence, a spread in the grain impact velocities v_G at a given location (due to a spread in orbital geometries) may contribute to the width of the histogram of the observed V_0^2. Since we have attributed this width to a spread in grain

size, the fractional dispersion of the grain size distribution 0.1–0.3 derived in this study may be an overestimate. Conversely, the fractional dispersion in impact velocities is expected to be smaller than about $6/(2\beta + 1)$ times the above value, i.e., $\Delta v_G/v_G \lesssim 0.07$–$0.2$. (Note that these inferences neglect a possible systematic relation between size and velocity.)

Finally, note that a systematic change of impact velocity with distance from the ring plane might change the vertical profile observed; for this effect to be an alternative explanation of the measured small thickness, the impact velocity v_G should systematically decrease with vertical distance, by about 7% over 4000 km.

APPENDIX

The PRA receiver was designed to measure polarized radio emissions in the following way: when the voltages on the two monopoles are respectively V_1 and V_2, it detects the sums $V_R^2 = |V_{R1} \pm iV_{R2}|^2 = |V_1 \pm iV_2|^2/\Gamma^2$, where Γ^2 is the receiver's transfer gain and the symbol $\pm$ corresponds to the right or left polarization. If the signal is symmetrical (for example a nonpolarized radio emission), the power spectrum at the receiver ports is thus given by

$$V_R^2 = V^2 \times |1 + i|^2/\Gamma^2 \approx 2V^2/\Gamma^2, \tag{35}$$

where V^2 is the corresponding power spectrum on each monopole.

From preflight calibrations, the output signal scale was defined in the following way: a white noise signal of spectral density $V_R = 1\ \mu\text{V kHz}^{-1/2}$ applied at one of the receiver ports in a given low-frequency channel produces an output signal $x = 23$ dB. This corresponds to

$$V_R^2 = (10^{-6})^2/10^3 = 10^{-15}\ \text{V}^2\ \text{Hz}^{-1}.$$

Since $V_R^2 \propto 10^{x/10}$ (for signals much above the receiver's noise), we deduce

$$V_R^2 = 5 \times 10^{-18} \times 10^{x/10}. \tag{36}$$

The corresponding voltage power spectral density V^2 on a monopole is deduced by using Eq. (35), whence

$$V^2 \approx 10^{-17} \times 10^{x/10} \times \Gamma^2/4 \tag{37}$$

(for signals much above the receiver's noise).

Let us now evaluate the gain Γ^2. In usual conditions, the signal is produced by voltages on the antennae. Let C_a be the capacitance of each monopole and C_b be the "base" capacitance which lumps together the receiver input capacity and that of the antenna erecting mechanism. Ground measurements suggest that $C_b \approx C_a$ (Lang and Peltzer 1977). Hence, when the potential on a monopole is V_1, the corresponding value at the receiver is reduced as $V_{R1} = V_1/\Gamma$ with $\Gamma = (C_a + C_b)/C_a \approx 2$, i.e., $\Gamma^2 \approx 4$. (This assumes that the antenna and receiver impedances are mainly capacitive, which is true for the frequencies of interest here.) The above relation holds for each monopole. In this case, (37) reduces to

$$V^2 \approx 10^{-17} \times 10^{x/10} \equiv V_0^2\ (\Gamma^2 \approx 4). \tag{38}$$

Since a reliable calibration is essential in this study, we check this result by using an independent method, based on common observations of solar bursts by Voyager PRA and the radio receiver on board ISEE-

3 (Lecacheux *et al.* 1989). These authors find that PRA and ISEE-3 observations agree within 20% (for similar viewing geometries) when the PRA output signal x is related to the flux of the (unpolarized) radio source by the relation

$$S(\mathrm{Wm^{-2}\,Hz^{-1}}) = 1.55 \times 10^{-21} \times 10^{x/10} \qquad (39)$$

(for emissions much above the receiver's noise, and at frequencies much above the ambient plasma frequency).

For an unpolarized source, the squared voltage on a short monopole of electric length l_e is related to the flux density by the relation

$$V^2 = 60\pi S l_e^2. \qquad (40)$$

The electric length of a Voyager monopole antenna has been measured recently by the rheographic method, using a scale model of the Voyager spacecraft (Lecacheux and Manning 1995). The result is $l_e = 5.8$ m. It is not surprising that this value be significantly different from the physical length, since the antennae are tilted on the spacecraft symmetry plane, and the spacecraft itself can hardly be approximated by its symmetry plane. Substituting the above value in (39) and (40), we get the same result as Eq. (38).

The calibration (38), given by two independent methods, holds when the following conditions are met: (i) the signal is much above the receiver's noise (which is true in the present study) and (ii) the receiver's transfer gain $\Gamma^2 \approx 4$; i.e., the voltage at the receiver ports is halved by the presence of the base capacitance. When the gain is different, which is the case in the present study, one uses

$$V_0^2 = V^2 \times 4/\Gamma^2 = 10^{-17} \times 10^{x/10}. \qquad (41)$$

REFERENCES

Aubier, M. G., N. Meyer-Vernet, and B. M. Pedersen 1983. Shot noise from grain and particle impacts in Saturn's ring plane. *Geophys. Res. Lett.* **10,** 5–8.

Burns, J. A., M. R. Showalter, and G. Morfill 1984. The etheral rings of Jupiter and Saturn. In *Planetary Rings* (R. Greenberg and A. Brahic, Eds.), pp. 200–272. Univ. of Arizona Press, Tucson.

Drapatz, S., and K. W. Michel 1974. Theory of shock-wave ionization upon high-velocity impact of micrometeorites. *Z. Naturforsch A* **29,** 870–879.

Fechtig, H., E. Grun, and J. Kissel 1978. Laboratory simulation. In *Cosmic Dust* (J. A. M. McDonnell, Ed.), pp. 607–664. Wiley, New York.

Goller, J. R., and E. Grun 1989. Calibration of the Galileo/Ulysses dust detectors with different projectile materials and at varying impact angles. *Planet. Space Sci.* **37,** 1197–1206.

Goller, J. R., E. Grun, and D. Maas 1986. Simulations of particle impacts on an impact ionization detector (DISDY IPM-P). In *20th Symp. on the Exploration of Halley's Comet* (B. Battrick, E. J. Rolfe, R. Reinhard, Eds.), pp. 333–336. ESA SP-250.

Grun, E. 1984. Impact ionisation from Gold, Aluminum and PCB-Z. In *The Giotto Spacecraft Impact-Induced Plasma Environment* (E. Rolfe and B. Battrick, Eds.), pp. 39–41. ESA SP-224.

Grun, E., E. Bussoleti, A. Minafra, H. Kuczera, and J. A. M. McDonnell 1984. First calibration measurements with the dust impact detector DISDY-IPM. *Adv. Space Res.* **4,** 291–295.

Gurnett, D. A., W. S. Kurth, L. J. Granroth, and S. C. Allendorf 1991. Micron-sized particle detected near Neptune by the Voyager 2 plasma wave instrument. *J. Geophys. Res.* **96,** 19,177–19,186.

Gurnett, D. A., E. Grun, D. Gallagher, W. S. Kurth, and F. L. Scarf 1983. Micron-sized particle detected near Saturn by the Voyager plasma wave instrument. *Icarus* **53,** 236–254.

Gurnett, D. A., W. S. Kurth, F. L. Scarf, J. A. Burns, J. N. Cuzzi, and E. Grun 1987. Micron-sized particle impacts detected near Uranus by the Voyager 2 plasma wave instrument. *J. Geophys. Res.* **92,** 14,959–14,968.

Hamilton, D. P. 1993. Motion of dust in a planetary magnetosphere: Orbit-averaged equations for oblateness, electromagnetic, and radiation forces with applications to Saturn's E ring. *Icarus* **101,** 244–264.

Hamilton, D. P., and J. A. Burns 1994. Origin of Saturn's E ring: self-sustained, naturally. *Science* **264,** 550–553.

Havnes, O. 1988. A streaming instability interaction between the solar wind and cometary dust. *Astron. Astrophys.* **193,** 309–312.

Horanyi, M., J. A. Burns, and D. P. Hamilton 1992. The dynamics of Saturn's E ring particles. *Icarus* **97,** 248–259.

Hornung, K., and S. Drapatz 1981. Residual ionisation after impact of large dust particles. In *The Comet Halley Probe Plasma Environment* (N. Longdon, Ed.), pp. 23–37. ESA SP-155.

Humes, D. H., R. L. O'Neal, W. H. Kinard, and J. M. Alvarez 1980. Impacts of Saturn's ring particles on Pioneer 11. *Science* **207,** 443–444.

Kaiser, M. L., M. D. Desch, W. S. Kurth, A. Lecacheux, F. Genova, B. M. Pedersen, and D. R. Evans 1984. Saturn as a radio source. In *Saturn* (T. Gehrels and M. S. Matthews, Eds.), pp. 378–415. Univ. of Arizona Press, Tucson.

Kruger, F. R., and J. Kissel 1984. Experimental investigations on ion emission with dust impact on solid surfaces. In *The Giotto Spacecraft Impact Induced Plasma Environment* (E. Rolfe and B. Battrick, Eds.), pp. 43–48. ESA SP-224.

Lang, G. J., and R. G. Peltzer 1977. Planetary radio astronomy receiver. *IEEE Trans.* **AES-13,** 466–471.

Lecacheux, A., and R. Manning 1995. Calibration of the Voyager planetary radioastronomy experiment by using the rheographic method. *Chapman Conf.* (*Santa Fe*).

Lecacheux, A., J. L. Steinberg, S. Hoang, and G. A. Dulk 1989. Characteristics of type III bursts in the solar wind from simultaneous observations on board ISEE-3 and Voyager. *Astron. Astrophys.* **217,** 237–250.

Meyer-Vernet, N. 1983. Quasi-thermal noise corrections due to particle impacts or emission. *J. Geophys. Res.* **88,** 8081–8093.

Meyer-Vernet, N. 1985. Comet Giacobini-Zinner diagnosis from radio measurements. *Adv. Space Res.* **5,** 37–46.

Meyer-Vernet, N., and C. Perche 1989. Tool kit for antennae and thermal noise near the plasma frequency. *J. Geophys. Res.* **94,** 2405–2415.

Meyer-Vernet, N., M. G. Aubier, and B. M. Pedersen 1986a. Voyager 2 at Uranus: Grain impacts in the ring plane. *Geophys. Res. Lett.* **13,** 617–620.

Meyer-Vernet, N., P. Couturier, S. Hoang, C. Perche, J. L. Steinberg, J. Fainberg, and C. Meetre 1986b. Plasma diagnosis from thermal noise and limits on dust flux or mass in Comet Giacobini-Zinner. *Science* **232,** 370–374.

Oberc, P. 1994. Dust impacts detected by Voyager-2 at Saturn and Uranus: a post-Halley view. *Icarus* **111,** 211–226.

Pang, K. D., C. Voge, J. W. Rhoads, and J. M. Ajello 1984. The E ring of Saturn and satellite Enceladus. *J. Geophys. Res.* **89,** 9459–9470.

Pedersen, B. M., N. Meyer-Vernet, M. G. Aubier, and P. Zarka 1991. Dust distribution around Neptune: Grain impacts near the ring plane measured by the Voyager radioastronomy experiment. *J. Geophys. Res.* **96,** 19,187–19,196.

Richardson, J. D., and E. C. Sittler 1990. A plasma density model

for Saturn based on Voyager observations. *J. Geophys. Res.* **95,** 12,019–12,031.

SHOWALTER, M. R., J. N. CUZZI, AND S. M. LARSON 1991. Structure and particle properties of Saturn's E ring. *Icarus* **94,** 451–473.

TSINTIKIDIS, D., W. S. KURTH, D. A. GURNETT, AND D. A. BARBOSA 1995. Study of dust in the vicinity of Dione using the Voyager 1 plasma wave instrument. *J. Geophys. Res.* **100,** 1811–1822.

TSINTIKIDIS, D., D. GURNETT, L. J. GRANROTH, S. C. ALLENDORF, W. S. KURTH, AND D. A. BARBOSA 1994. A revised analysis of micron-sized particles detected near Saturn by the Voyager 2 plasma wave instrument. *J. Geophys. Res.* **99,** 2261–2270.

WARWICK, J. W., J. B. PEARCE, R. G. PELTZER, AND A. C. RIDDLE 1977. Planetary radio astronomy experiment for Voyager missions. *Space Sci. Rev.* **21,** 309–327.